Journal Pre-proofs

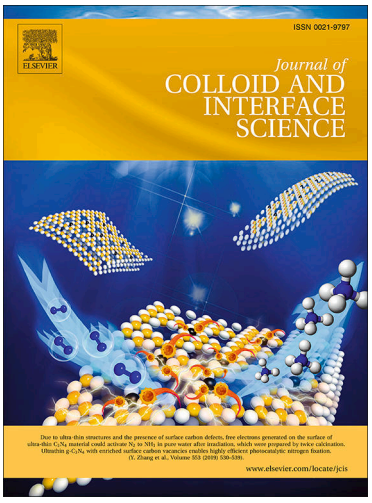

Tuning and transferring slow photons from TiO_2 photonic crystals to $BiVO_4$ nanoparticles for unprecedented visible light photocatalysis

Thomas L. Madanu, Sébastien R. Mouchet, Olivier Deparis, Jing Liu, Yu Li, Bao-Lian Su

PII: S0021-9797(22)02176-2
DOI: https://doi.org/10.1016/j.jcis.2022.12.033
Reference: YJCIS 31454

To appear in: *Journal of Colloid and Interface Science*

Received Date: 14 October 2022
Revised Date: 28 November 2022
Accepted Date: 7 December 2022

Please cite this article as: T.L. Madanu, S.R. Mouchet, O. Deparis, J. Liu, Y. Li, B-L. Su, Tuning and transferring slow photons from TiO_2 photonic crystals to $BiVO_4$ nanoparticles for unprecedented visible light photocatalysis, *Journal of Colloid and Interface Science* (2022), doi: https://doi.org/10.1016/j.jcis.2022.12.033

Tuning and transferring slow photons from TiO_2 photonic crystals to $BiVO_4$ nanoparticles for unprecedented visible light photocatalysis

Thomas L. Madanu[a], Sébastien R. Mouchet[b, c], Olivier Deparis[b], Jing Liu[d], Yu Li[d] and Bao-Lian Su[*a, d]

[a] Laboratory of Inorganic Materials Chemistry (CMI), University of Namur, Rue de Bruxelles, 61-B-5000 Namur, Belgium.

[b] Solid-State Physics Laboratory & Namur Institute of Structured Matter (NISM), University of Namur, Rue de Bruxelles, 61-B-5000 Namur, Belgium.

[c] School of Physics, University of Exeter, Physics building, Stocker Road, Exeter EX4 4QL, UK

[d] State Key Laboratory of Advanced Technology for Material Synthesis and Processing, Wuhan University of Technology, Wuhan, 430070, Hubei, China

* Bao-Lian Su

Email: bao-lian.su@unamur.be; Fax: +32 81 725414; Tel: +32 81 724531

Thomas Lourdu Madanu: Conceptualization, Methodology, Investigation, Formal analysis, Writing-original draft preparation. **Sebastien Mouchet:** Formal analysis, Writing-review & editing. **Olivier Deparis:** Formal analysis, Resources, **Jing Liu**: Writing-review & editing, **Yu Li**: Writing-review & editing, **Bao-Lian Su:** Conceptualization, Supervision, Visualization, Project administration.

Abstract

Periodic structures with alternating refractive indices such as inverse opal photonic crystals are capable of reducing the group velocity of light such that this slowed light can be more efficiently harvested for highly enhanced solar energy conversion. However, the generation, the manipulation and, in particular, the practical applications of these slow photons remain highly challenging. Here, we report the first proof of concept on the ability to control, in an inverse opal TiO_2-$BiVO_4$ hetero-composite, the transfer of slow photons generated from the inverse opal photonic structure to the photocatalytically active $BiVO_4$ nanoparticles for highly enhanced visible light photoconversion. Tuning the slow photon frequencies, in order to accommodate the electronic band gap of $BiVO_4$ for slow photon transfer and for significantly improved light harvesting, was successfully achieved by varying the structural periodicity (pore size) of inverse opal and the light incidence angle. The photocatalytic activity of $BiVO_4$ in all inverse opal structures, promoted by slow photon effect, reached up to 7 times higher than those in the non-structured compact films. This work opens new avenues for the practical utilization of slow photon effect under visible light in photocatalytic energy-related applications like water splitting and carbon dioxide reduction and in photovoltaics.

Keywords: Photocatalysis, angle-resolved photocatalysis, inverse opals, photonic crystals, slow photons, visible light, light harvesting, TiO_2 (titania), $BiVO_4$ (bismuth vanadate).

1. Introduction

Harnessing solar energy for photocatalytic energy conversion is a pressing global challenge. In the recent past, significant advances have been made in choosing and modifying materials to improve photocatalytic performance[1-3]. However, modifying light for improved light-matter interaction in photocatalysis remains largely underexplored. Inverse opal (IO) photonic structures are among the most promising light-manipulating materials for photocatalytic applications, thanks to their fascinating and exclusive property of slow photon effect (SPE)[4,5]. Having periodic structures with alternating refractive indices, they are capable of influencing the propagation of photons such that light at a certain wavelength is reflected, creating a photonic stop band gap (SBG), while the group velocity of light at lower and higher frequency edges (blue and red) of the SBG is reduced nearly to zero[6-9]. Such photons, called "slow photons" form a standing wave within the material[10]. When the spectral regions of these slow photons are accurately tuned to overlap with the electronic absorption of the semiconductor, these "confined photons" could be efficiently harvested to improve light energy conversion in photocatalytic, photovoltaic and photoelectrochemical devices[11-14]. To maximize the utilization of slow photon effect, tuning strategies including the variation of parameters like lattice constant (related to pore diameter), effective refractive index (RI), filling fraction and angle of incidence can be employed to modulate slow photon frequencies.

In the past two decades, various attempts have been made to test IO structures for photocatalysis. Many of them claimed the contribution of slow photons in photocatalytic enhancement, but very few unambiguously established it[15]. The first attempt to demonstrate SPE in photocatalysis was realized in IO TiO_2 for the solid phase photodegradation of methylene blue (MB) by measuring activity at different angles using IO samples with different pore sizes[16]. Later on, researchers probed SPE on IO TiO_2 for Rhodamine B (RhB) degradation in aqueous phase[17,18]. This was a significant improvement since most industrial photocatalytic reactions are carried out in aqueous phase wherein the change in slow photon frequencies with change in medium needs to be considered. Similarly, SPE was also studied in other materials such as IO Fe_2O_3[19], IO Bi_2WO_6[20] and IO ZnO[21]. Recently, it was explored again in IO TiO_2 for aqueous-phase MB degradation[22] and solid-state stearic acid degradation[23] with supportive evidence from simulation studies. The above works, which reported photocatalytic enhancement factors ranging from 2 to 4, between IO structured photocatalysts and their non-structured counterparts were, however, limited to single component photocatalysts, most of

them responsive only in the UV region. Exploiting slow photons for visible light photocatalysis becomes an urgent and compelling research subject of current interest.

Although IO structures of visible light responsive semiconducting materials such as simple oxides (e.g. WO_3, Fe_2O_3, Cu_2O etc.), complex oxides (e.g. $BiVO_4$, Fe_2TiO_5), nitrides (e.g. C_3N_4, Ta_3N_5) and sulphides (e.g. CdS, SnS, SnS_2) can be used, the difficulty involved in preparing IO structures of these compounds with tunable photonic properties along with the lack of satisfactory experimental protocols for preparing long-range ordered structures, renders them less effective for the maximum utilization of slow photon effect. Also, the toxicity of some materials like sulphides, impede the implementation of practical research. In addition, forming heterocomposite systems of IO photocatalysts with noble precious metals, which has often been employed to improve visible light harvesting, increases the cost involved in photocatalyst synthesis. The best and realistic scenario is to combine the relatively easy-to-fabricate IO photonic structure of TiO_2, with a low cost, non-toxic and highly visible light-responsive semiconducting material.

We report here, for the first time, the utilization of slow photons in a visible-light active, bi-component IO TiO_2-$BiVO_4$ (ITBV) hetero-composite photocatalyst system, chosen in our work to serve as a proof of concept, for highly enhanced photocatalytic performance. Such a concept involving the generation of slow photons by the IO structure, tuning their frequencies through lattice constant and light incidence angle variations and transferring them to the composited visible light semiconductor for photocatalytic enhancement, particularly in aqueous phase, was never proved either theoretically or experimentally. The photocatalytic reaction was realized using a series of IO TiO_2-$BiVO_4$ samples having varying lattice constants (pore sizes) at increasing light incidence angles in aqueous solutions. The four to seven-fold increase in efficiency of all IO TiO_2-$BiVO_4$ samples under slow photon-assisted tuning conditions compared to their non-IO counterparts, firmly established and confirmed our ability to tune and transfer slow photons in visible light-responsive IO photonic composite materials for photocatalytic enhancement. This experimentally proved concept was further theoretically justified by Rigorous Coupled Wave Analysis (RCWA) simulation. Through this work, we envisage that more efficient pathways using slow photon effect can be successfully explored and implemented to solve the current problem of low light harvesting efficiency in all solar energy conversion technologies.

2. Experimental materials and methods

Materials

Styrene (99%) and Titanium (IV) isopropoxide (TIP) (98+%) were purchased from Acros Organics; potassium persulfate ($K_2S_2O_8$) (≥ 99%), tetramethylammonium hydroxide (TMAH) (purity titration by HCl (M) = 0.98 – 1.02 M) and 2-propanol (≥99.5%) from Sigma Aldrich; bismuth (III) nitrate pentahydrate ($Bi(NO_3)_3.5H_2O$) (≥98%) and ammonium monovanadate (NH_4VO_3) (≥99.8%) from Carl Roth; polyvinylpyrrolidone (PVP) from TCI Chemicals and Rhodamine B (RhB) from Alfa Aesar. Polystyrene (PS) suspension of colloids for quality comparison PS 350 (D = 370 nm) was ordered from Polysciences, Inc. while PS 460 (D = 460 nm) was procured from Sigma Aldrich. The procured chemicals were used without further purification. Microscope glass slides were obtained from VWR and cut to 1.85×1.25 cm^2.

Synthesis of colloidal polystyrene colloids

PS colloids of 370, 420 and 460 nm bead sizes were synthesized by emulsion polymerization method using a previously reported method[24] by varying the proportions of styrene monomer, PVP emulsifier and $K_2S_2O_8$ initiator added (Table ST1 in supporting information (SI)). The synthesized colloids were then subjected to gradient centrifugation in order to improve the monodispersity of the colloids. The graded colloids were redispersed in water to obtain a 5 wt.% dispersion and stored at 10^{o}C for further use.

Synthesis of TiO_2 sol

Amorphous-crystalline bi-phase TiO_2 sol and subsequently the IO structures were prepared by adapting a recently reported synthesis method[25]. In a typical peptization process, 90 ml of water was initially taken in a 250 ml double neck round bottom flask and placed in an ice bath before dissolving 0.8141 ml (0.8263 g) of TMAH. 1.1 ml of TIP, such that the molar ratio TIP/TMAH = 1.6, was dispersed in 15 ml of 2-propanol and then added drop by drop to the above solution under constant stirring. A milky white precipitate was formed which disappeared later under reflux. The solution was left to stir for 15 minutes and then transferred to a silicone oil bath pre-heated to 105^{o}C where it was left to reflux for six hours. The solution was later cooled and used within an ageing period of 3 to 10 days.

Inverse Opal TiO_2 (IT) thin film synthesis

Inverse opal TiO_2 structures were prepared by evaporation assisted self-coassembly of TiO_2 matrix and PS colloids on a glass substrate followed by calcination. To prepare the coassembly solution, 0.1 wt% of PS colloids were dispersed in water to which 40 µl/mL of the TiO_2 sol

was added. A glass substrate, after being previously treated with piranha solution (3:1 H_2SO_4/H_2O_2) (caution: highly corrosive) to render the surface hydrophilic, washed with distilled water and dried under N_2 gas, was vertically suspended in the coassembly solution using clips and left in an oven at 40^oC for two days. The co-assembled sample was then calcined at 500^oC for two hours at a ramp rate of 1^oC/min to give IO TiO_2 film with well-defined thickness.

Inverse opal TiO_2-$BiVO_4$ (ITBV) composites

$BiVO_4$ nanoparticles were deposited on IO TiO_2 thin films by optimizing a Sequential Ionic Layer Adsorption Reaction (SILAR) method, also termed as Chemical Bath Deposition (CBD) method[26]. Four solutions were initially prepared for $BiVO_4$ deposition: a) 0.742 x 10^{-3} moles of $Bi(NO_3)_3.5H_2O$ dissolved in a solution of 30 ml water containing 3 ml acetic acid b) 30 ml water containing 3 ml acetic acid c) 1.453 x 10^{-3} moles of NH_4VO_3 dissolved in 30 ml water at 60^oC and d) 30 ml water. The IO TiO_2 substrate was first dipped in solution (a) for 20 s to adsorb Bi^{3+} ions, rinsed in (b) for 5 s to remove loosely adsorbed ions, then dipped in (c) for 20 s to adsorb VO_4^{3-} ions and rinsed in (d) to remove loosely adsorbed ions. This entire cycle was repeated for 20 times to obtain optimum deposition of cationic and anionic parts. The substrate was then dried and calcined at 500^oC to obtain the crystalline phase of $BiVO_4$ nanoparticles.

TiO_2, $BiVO_4$ and TiO_2-$BiVO_4$ films

Compact films of TiO_2 (T), $BiVO_4$ (BV) and TiO_2-$BiVO_4$ (TBV) were prepared and tested for photocatalytic activity in order to be compared with ITBV samples. TiO_2 films[27] and $BiVO_4$ films[28] were prepared by optimizing sol-gel dip coating methods reported previously. To obtain TiO_2-$BiVO_4$ films, the as-prepared TiO_2 films were deposited with $BiVO_4$ using the same chemical deposition method used for the synthesis of ITBV samples.

Characterization

Size distribution and the related coefficient of variation (CV) to estimate monodispersity of the synthesized PS colloids were calculated using data from Dynamic Light Scattering (DLS) NanoPlus HD zeta/nanoparticle analyser. Scanning Electron Microscope (SEM) images along with the corresponding Energy Dispersive X-ray Spectroscopy (EDS) for elemental mapping and quantitative analysis were taken using a JEOL JSM-7500F SEM equipped with an X-ray analysis probe at an accelerating voltage of 20kV. Transmission Electron Microscope (TEM)

images and High-Angle Annular Dark-Field Imaging (HAADF) imaging and mapping were done using Tecnai G^2 20LaB6 TEM operating at 200 kV equipped with Bruker X-flash 6Ti30 detector. Atomic Force Microscope (AFM) images were recorded in tapping-mode using Nanoscope III, BrukerTM, with Si cantilevers (Nanosensors PPP-NCHR) having a resonance frequency around 290 kHz, a nominal spring constant of 42 N/m, and an integrated Si tip with a nominal apex radius of curvature lower than 10 nm. X-ray diffraction (XRD) patterns were obtained from PANalytical X'PERT PRO Bragg-Brentano diffractometer using Cu Kα radiation (λ = 1.54184 Å) measured in 2θ angle range 20°-60°. Absorptance measurements were taken using a Perkin Elmer 750S UV/Vis/NIR spectrophotometer after calibration with a Labsphere SRS-99-020 white reference. The optical microscopic images and the associated micro-spectrophotometric reflectance measurements were obtained using an Olympus BX 61 microscope fitted with an Olympus XC50 camera and a halogen Osram HLX 64625 visible light source. The micro-spectrophotometric reflectance (normalized with respect to the intensity reflected by an Avantes WS-2 white diffusor) was measured with an Ocean optics QE65 Pro spectrophotometer connected to the microscope. The variation of reflectance with incident angle was measured with an Avantes AvaSpec-2048-2 spectrophotometer coupled with an AvaLight-DH-S-BAL deuterium-halogen light source after calibrating with an Avantes WS-2 white diffusor. An Avantes AFH-15 fibre holder allowing the variation of angle of incidence and detection from 0^o to 75^o in steps of 15^o was used to mount the probe. For measurements at normal incidence, a bifurcated optical fibre was used to guide incident and reflected light, whereas for measurements at non-normal incidence, two optical fibres, in specular configuration, with one connected to the light source and the other to the spectrophotometer, were used.

Photocatalytic testing

Photocatalytic degradation was carried out using a home-made device with a 300 W ELDIM-RFLX-ET101-01 EZ Reflex light source emitting a spectral range of 390-770 nm. Light was channelled through an Avantes FC-UV-200 optical fibre mounted on Avantes AFH-15 fibre holder. Absorbance of RhB solutions was determined using Varian Cary 5000 UV-Vis-NIR (UV 1001M187) and Bio-Tek Instruments UVIKON XS UV-Visible spectrophotometers in the spectral range of 400-700nm. For photocatalytic degradation, the sample was immersed in 4 ml of 2.5 μM RhB solution and left in the dark for 30 minutes to reach equilibrium. The distance between the end of the optical fibre and the sample was adjusted such that the spot size of illumination of the catalyst was ca. 1 cm in diameter. The experiments were conducted

at 0°, 15°, 30° and 45°, each for six hours, during which 1 ml of the solution was taken out every 30 minutes for absorptance measurement and returned to the solution immediately. Comparison between the photocatalytic activities of all samples was done after normalization with respect to the weight of the photocatalyst deposited on the substrate, and from the weight fractions of TiO_2 and $BiVO_4$ deposited, estimated from EDS elemental mass composition data.

3. Results and discussion

Stop band gap tuning

Tuning the photonic stop band gap and the slow photon frequencies, in order to improve light harvesting, was achieved by varying both the lattice constant (pore size) of the inverse opals and the light incidence angle. Highly ordered IO structures are required for manifesting a tunable SBG, which in turn requires the usage of highly monodisperse template colloids and an optimal method for their ordered self-assembly on the substrate[29,30]. DLS measurements revealed that the synthesized PS colloids were of high quality with excellent monodispersity (Fig. S1 (a-c)). The one-step coassembly of the template colloids and the bi-phase amorphous-crystalline TiO_2 sol, helped in reducing crack formation, and resulted in a homogeneous, highly ordered self-assembly of the colloid-TiO_2 sol on glass substrates (Fig. S1 (d-f)).

SEM images in Figs. 1(a-b, e-f, i-j), and S2 indicate that the IO structures obtained after calcination possessed a high degree of structural order over a long range. Diameters of the air spheres were measured to be 258, 286 and 323 nm (±10 nm) for IO structures prepared from PS colloids of 370, 420 and 460 nm respectively. The average 30% shrinkage of pore size compared to original colloid size can be attributed to the formation of much condensed crystalline phase of TiO_2[31,32]. The inset optical microscope images in Fig. 1 (a, e, i) show long-range distinct colours of the inverse opals (violet, blue and green, respectively) produced by the stop band gap reflection whose wavelength red shifts with increase in lattice constant (pore size).

TEM images of IT 370 at different magnifications (Fig. 1 (q-s)) not only confirm the high degree of order in the IO structure but also reveal the size of the nanocrystal blocks that compose the TiO_2 framework, which was measured to be about 20-30 nm. Their size and shape were found to vary significantly with the synthesis parameters and ageing period of the TiO_2 sol (Fig. S3). The nanocrystal blocks introduced additional inter-particular mesopores of around 2-5 nm, which rendered the filling fraction of TiO_2 lower than the ideal value of 0.26 in a hexagonal close packed system, which could be as low as 0.12 based on previous reports[17].

Consequently, the position of the SBG blue-shifted compared to that of the expected ideal structure, since the effective refractive index of the photocatalyst was reduced. Thickness of the IO film, which varies with colloid concentration, is of considerable significance since it impacts the photonic properties by broadening the SBG reflection peak with increasing thickness[33,34]. Cross-section images of the IO films (Fig. 1 (c, g, k)) revealed that the average thickness of the film was about 2 μm with the concentration of colloids used being 0.1 wt%. The number of layers was well controlled to vary from 6 to10, generally decreasing with increase in colloid size and increasing with increase in colloid concentration.

Tunability of the stop band gap with incidence angle was verified by measuring angle-resolved reflectance spectra of IT 370, IT 420 and IT 460 in air medium (Fig. 1 (d, h, l)). In each case, the distinct SBG reflection peak red shifted with increase in pore size and blue shifted with increase in incidence angle. This confirmed not only that the synthesized IO TiO_2 samples exhibited excellent photonic properties but also that the highly ordered structures permitted exceptional controllability of the slow photon wavelengths. The TiO_2 compact film synthesized for comparison (Figs. 1 (m-o), S11), with ≈ 1 μm thickness and nanocrystal size of 20-40 nm, as estimated from its TEM image (Fig. 1 (t)), did not show any photonic properties, as evidenced from the absence of a distinct SBG peak in the reflectance spectra (Fig. 1 (p)).

Creating a hetero-composite of IO TiO_2 with the highly visible light photoactive $BiVO_4$, was carried out by a controlled SILAR method[26] with 20 cycles of deposition, that avoided the formation of overlayer and provided an optimum balance between improved light absorption in the visible range and simultaneous retention of photonic properties (Fig. S4). SEM images (Fig. 2 (a-b, d-e, g-h)) and AFM images (Fig. S6) reveal that $BiVO_4$ was evenly deposited on IO TiO_2, albeit the presence of randomly agglomerated crystals of $BiVO_4$. In addition, EDS elemental mapping carried out in TEM (Fig. 2 (m-q)) and in SEM (Figs. S7-S9)) revealed a very homogeneous dispersion of Bi and V across IO TiO_2. EDS elemental analysis was used to quantify the deposition of $BiVO_4$, which was, on an average, 25% by molecular weight with reference to TiO_2 (Table ST2). From the SEM images, it was obvious that the IO composite structures retained their highly ordered structures after $BiVO_4$ deposition and subsequent calcination. The optical microscope images of ITBV 370, ITBV 420 and ITBV 460 (Fig. 2 (a, d, g), inset) and their angle-resolved reflectance measurements in air (Fig. 2 (c, f, i)) were observed to be very similar to those of their respective IO TiO_2 counterparts, confirming that no noticeable change in photonic properties was recorded by the deposition process. Similar to the case of TiO_2 compact film, the reference TiO_2-$BiVO_4$ compact film (Figs. 2 (j, k), S11 (e,

f)) did not exhibit any photonic properties, but showed only the characteristic reflectance spectra corresponding to that of TiO_2-$BiVO_4$ composite (Fig. 2 (l)).

XRD patterns (Fig. 3 (a)) confirmed that TiO_2 was present predominantly in the anatase phase (with traces of rutile phase) while $BiVO_4$ was present in the monoclinic phase. Based on XRD data, calculation of the approximative crystallite sizes was done using Scherrer equation. The crystallite sizes of TiO_2 and $BiVO_4$ in ITBV films were calculated to be 14 nm and 23 nm while those in TBV, BV and T compact films were 28 nm and 35 nm respectively. UV-Visible absorptance measurements of the three IO TiO_2-$BiVO_4$ films and their comparison with TiO_2, $BiVO_4$ and TiO_2-$BiVO_4$ compact films (Fig. 3 (b)) indicated that the absorptance of all ITBV composites as well as that of TBV compact film shifted to the visible range owing to the narrow electronic band gap (EBG) of $BiVO_4$, rendering them efficient for visible light photocatalysis.

As photocatalytic activities were to be tested in aqueous medium, the investigation of photonic properties in water compared with those in air is essential. The optical images taken on the same IO domains in air and under water clearly show a red shift in colour with change in medium (Fig. 3 (c-h)). Compared to the spectra in air (Fig. 2 (c, f, i)), all the SBG peaks red-shifted under water, due to the increase in effective RI of the system caused by the increase in RI of the pore-filling medium (from $n_{air} = 1$ to $n_{water} = 1.33$). The effect of the medium on the position of SBG and hence on that of the slow photons is evident. As in the case of air medium, reflectance measurements in water showed that the SBG peak red-shifted with increase in pore size and blue-shifted with increase in incidence angle for all the three ITBV samples (Fig. 3 (i, j, k)). The intensity of the SBG reflection peak in water, however, was found to be relatively reduced compared to that in air, as indicated in micro-spectrophotometric measurements (Fig. S10). This attenuation in intensity in aqueous medium can be explained by the reduction in RI contrast between the pore-filling medium i.e. water and the IO material. Reflectance measurements of TiO_2-$BiVO_4$ compact film under water did not show any significant change in spectra with change in medium from air to water (Figs. 2 (l), 3 (l)).

Reflectance prediction using modified Bragg's law

The observations of shift in SBG peak position with pore size, incidence angle and pore-filling medium (Fig. 3(m)) were found to be consistent with theoretical predictions, simulations and previously reported experiments on optical properties of photonic crystals[35]. A modified Bragg equation[36],

$$\lambda_B = 2 \cdot \sqrt{2/3} \cdot D \cdot \sqrt{n_{eff}^2 - n_{inc}^2 \sin^2 \theta}$$

was used to estimate the effective refractive index (n_{eff}) of IO TiO_2-$BiVO_4$ by simultaneously fitting SBG peak positions (λ_B) of all the IO samples having different pore diameters (D), i.e., IO periodicities, measured at different incidence angles (θ), both in air and in water (incidence medium refractive index: n_{inc}). The effective RI was calculated using Bruggeman's formula[37,38] (assuming spherical pores) from the volume filling fraction (*f*) of material in the inverse opal, the RI of the composite material (n_{mat}) and the RI of the pore filling medium (n_{med}). A value of *f*=0.12, lower than the perfect IO close packing value (*f*=0.26), was inferred from the analysis of microscope images, which is consistent with previous reports[17,23]. The composite material RI was calculated as $n_{mat} = xn_1 + (1-x)n_2$, where n_1 and n_2 are the RI of porous TiO_2 and $BiVO_4$, while (x) and (1-x) are the volume fractions of TiO_2 and $BiVO_4$ (see SI for their approximation). Based on the above consideration and the calculation of wavelength-dependent complex RI using data reported for dense TiO_2[39] and dense $BiVO_4$[40], the RI (real part) of the porous TiO_2 and porous $BiVO_4$ materials (at λ=500 nm) were estimated to be 1.836 and 2.764 respectively (Fig. S20). The decrease in the estimated RI of the porous thin films compared to that of bulk TiO_2 and bulk $BiVO_4$ can be attributed to the decrease in density of the material, a fact established in previous reports through the correlation between density and RI in thin films[41,42]. As a result, for the composite material, n_{mat}=1.95 was obtained; this real and constant value was used in the modified Bragg formula. For data fitting related to optical measurements in water, Fresnel correction ($n_{inc} \neq n_{med}$) was applied in order to account for the refraction at the interface between air and water in the present experimental configuration. In addition, incomplete infiltration of the pores in water medium had to be considered and a RI value of $n_{med} = 1.20$ (60% water and 40% air) was found to give the best fit to the optical measurements in water. With the above factors taken into consideration, a nearly perfect fit was obtained between experimentally observed SBG peak positions and theoretically calculated ones, for all samples, at all angles, both in air and in water, as shown in Fig. 3(m). This accurate prediction of the SBG peak positions validated the procedure used for RI calculation.

RCWA simulations of reflectance and absorptance

The angular dependence of reflectance and absorptance spectra in IO slabs (Fig. 3 (n, o)) were predicted using the rigorous coupled wave analysis (RCWA). RCWA is a full vector, three-dimensional, electromagnetic computational method that is well suited to simulations of the optical response of inverse opals[23,43]. Spectra were calculated, at different incident polar angles

(θ), assuming fixed incident azimuth angle and non-polarized light. Calculations took into account contributions of all diffraction orders and evanescent waves[43]. RCWA, being based on Fourier series expansion of the permittivity in lateral directions, numerical convergence was checked with respect to the number of Fourier components (n_g), which is also equal to the number of plane waves in electric (magnetic) field expansions. We found that $n_g = 5 \times 5$ plane waves were sufficient to reach good accuracy. Simulated IO slabs ([111] crystal facet exposed to the surface) consisted of 4-unit cells that were stacked one over the other such that the slab thickness was close to the sample thickness in experiments. The parameter D of simulated IO slabs was taken equal to the pore diameters determined from SEM images (Table ST3). The same values of *f* and n_{med} used for Bragg fitting were used for RCWA. However, unlike for Bragg's equation predictions, the wavelength-dependent complex RI data were used in order to account for material's absorption and its spectral dependence.

RCWA reflectance simulations were found to be in excellent agreement with experimentally observed values of SBG peak wavelengths, both in air and in water, at all angles (Figs. 3 (o), S21). From reflectance simulations, the wavelengths of slow photons, at both blue and red edges of the SBG, were determined (Fig. S22). Absorptance spectra were also simulated at different angles for ITBV 370 in water, taken as an example, and compared with absorptance spectra of thin films of TiO_2, $BiVO_4$ and TiO_2-$BiVO_4$, whose thicknesses were calculated to lead to identical volume fractions of the corresponding materials in the ITBV samples (Fig. 3(n)). RCWA reflectance and absorptance simulations permitted not only the theoretical prediction of the exact position of slow photons but also the justification of photocatalytic activity based on the correlation between tuning of slow photon wavelengths and enhancement of light absorption.

Slow photon manipulation for photocatalysis

The ability to tune the wavelengths of slow photons for obtaining maximized photocatalytic activity was demonstrated through the photodegradation of RhB using a lab set-up device (Fig. 4(a-c)) using three IO TiO_2-$BiVO_4$ samples - ITBV 370, ITBV 420 and ITBV 460 - each at incidence angles 0°, 15°, 30° and 45°, and comparing them with the non-IO compact films - TiO_2-$BiVO_4$, $BiVO_4$, TiO_2 - and with the inverse opal TiO_2 (IT 420). This is the first experiment realized for a heterocomposite photonic visible light photocatalyst in a real working condition i.e. water. The comparison of normalized photocatalytic activities of all the samples is presented in terms of degradation efficiency ($(C_0 - C) \times 100 / C_0$) in Fig. 4 (d), variation

in RhB absorbtance with time in Figs. S12-S18, normalized RhB concentration (C_0/C) in Fig. S19 and in tabular form in Table ST3.

ITBV 370 exhibited a degradation efficiency of 65% at 0° incidence angle. However, with increase in incidence angle to 15°, 30° and 45°, the activity increased to 69%, 75% and 84% respectively (Fig. 4(d)). This can be explained by the shift of SBG reflection peak and the wavelengths of red edge slow photons with incidence angle (Fig. 3 (i)). At 0°, the red edge slow photons at ≈ 590 nm, generated by ITBV 370, were far away from the electronic absorption edge of $BiVO_4$. With increasing incidence angles in aqueous conditions, they underwent a gradual blue shift, closer to the electronic absorption of $BiVO_4$. At 45°, the wavelengths of red edge slow photons overlapped completely with the absorption region of $BiVO_4$. In this case, the photons at the red edge whose group velocity was drastically reduced and localized preferentially in the higher RI medium (IO material skeleton), were able to be more efficiently harvested by $BiVO_4$ nanoparticles resulting in significant improvement in photocatalytic activity. When compared to the degradation efficiency of non-IO compact films, this highest activity achieved by the accurate tuning and transfer of slow photons at 45° incidence angle was 3.5, 3.5 and 6 times higher than those of TiO_2-$BiVO_4$, $BiVO_4$ and TiO_2 compact films that did not manifest any distinct SBG with tunable slow photon regions at the edges (Figs. 1(l), 2(p), 3(l)). Additional conclusive evidence of the slow photon effect was drawn from the observation that the change in activity with incidence angle variation found in IO TiO_2-$BiVO_4$ samples was not present in the non-IO compact films (Fig. 4(d)). Further comparison was made with the IO TiO_2 sample (IT 420) without the $BiVO_4$ component. In this case, the activity of ITBV 370 at 45° incidence angle was 4.5 times higher than that of IT 420. This confirmed that, in our experimental conditions, $BiVO_4$ was the predominant contributor for light absorption and photodegradation, as the slow photons of the ITBV samples in aqueous medium were located in the visible range around the electronic absorption edge of $BiVO_4$ (ca. 516 nm = 2.4 eV) and far away from the electronic absorption edge of TiO_2 (ca. 387 nm = 3.2 eV).

Similarly, for ITBV 420, with increase in incidence angle, the degradation efficiency gradually increased to reach the highest activity of 97% at 30° incidence angle and then decreased at 45° incidence angle. In this case, the blue edge slow photons were tuned to the electronic absorption of $BiVO_4$ (Fig. 3 (j)). Photons at the blue edge with their reduced group velocity are localized preferentially in the lower RI medium (water). Although counter-intuitive to understand, these blue-edge slow photons, despite their preferential localization in water, were able to effectively

enhance absorption by $BiVO_4$ nanoparticles. This blue edge SPE was previously established and explained through both theoretical explanation based on optical simulations[43] and experimental results[44]. In fact, it was noted in our experiments that, among the three ITBV photocatalysts where tuning was actualized, ITBV 420 demonstrated the highest performance of 97% at 30° incidence angle. This can be explained by the interplay between two opposing factors in IO photocatalysis - increased light absorption due to slow photons and decreased light harvesting due to stop band gap reflection. In the case of ITBV 420 at 30° incidence angle, the blue edge slow photons were tuned to overlap with the electronic absorption of $BiVO_4$ while at the same time the SBG reflection peak remained outside the absorption region of the photocatalyst, thereby maximizing absorption and simultaneously avoiding reflection. This reasoning was further substantiated by the observation of a drop in degradation efficiency to 79% with further increase in incidence angle to 45°. At this angle, the SBG reflection peak further blue shifted to overlap with $BiVO_4$ absorption region causing light to be reflected, thereby attenuating the absorption of light by $BiVO_4$ and reducing the activity of the photocatalyst. The highest activity obtained under accurate tuning conditions in ITBV 420 was 4, 4, and 7 times higher than those of TiO_2-$BiVO_4$, $BiVO_4$ and TiO_2 compact films respectively.

ITBV 460 showed similar trends with the highest activity (85%) at 45° incidence where the blue edge slow photons overlapped with the electronic absorption of $BiVO_4$ (Fig. 3 (k)). At lower incidence angles, it exhibited lower photocatalytic activities as the slow photons were located at longer wavelengths, far away from the absorption region of $BiVO_4$. The manipulation of slow photons, in this sample, resulted in an increase in photocatalytic activity that was 3.5, 3.5 and 6 times higher than those of TiO_2-$BiVO_4$, $BiVO_4$ and TiO_2 compact films.

RCWA reflectance and absorptance simulations further validated the above interpretation of experimental results. In the case of ITBV 370, taken as an example, the red edge slow photons at 0° and 45° incidence angles, are highlighted by vertical dashed lines in the simulated absorptance spectra (Fig. 3(n)). It is observed that the red edge at normal incidence (θ=0°) lies beyond the electronic absorption edge of $BiVO_4$ (yellow shaded region in Fig. 3 (n)). On the other hand, the red edge at incidence angle equal to θ=45° lies well within the absorption of bismuth vanadate. This justifies the difference in the experimentally measured photocatalytic activity which was the highest at 45°, with slow photon assistance, and the least at 0°, without slow photon assistance. Furthermore, due to slow photons, ITBV 370 exhibited significantly higher absorptance than the compact films at all angles, in spite of slight attenuation of the absorptance in the spectral region of SBG angle-dependent reflection. This validates the

experimental observation wherein the photocatalytic activities of all IO samples were 4-7 times higher than their corresponding equivalent compact films (Fig. 4(d)). RCWA simulations, by quantitatively predicting the total absorption of the samples, enabled us to rationalize the accurate correspondence between theoretical and experimental results in terms of the activities of all the samples. In addition, the reflectance and absorptance spectra predicted by RCWA permitted us to justify the correspondence between the slow photon tuning conditions, their transfer from the IO TiO_2 structure to the photoactive $BiVO_4$ composite and the enhancement of absorption that led to highly increased photocatalytic activity.

The IO TiO_2-$BiVO_4$ photocatalyst was verified for morphological stability by analysing the images in SEM after photocatalysis. The IO structure of one of the samples, ITBV 370, shown in Fig. S23 (a), revealed that the structure remained relatively stable after four cycles of photocatalysis, each for six hours. Photocatalytic consistency was verified by additional photocatalytic tests using the same sample, ITBV 370, for four further cycles at the same light incidence angle of 0^o. The results, as shown in Fig. S23 (b-c), indicated that was no significant difference in photocatalytic activity.

The above experimental results, firmly supported by simulations studies, establish the feasibility to generate, control, tune and transfer slow photons from IO TiO_2 structures to the composited $BiVO_4$ nanoparticles for highly enhanced visible light photocatalysis. Further, from the above data, it can be generalized that photocatalytic efficiency can be drastically improved by using inverse opal semiconductor photocatalysts, particularly by accurately tuning the wavelengths of slow photons to the electronic absorption of the photocatalyst while simultaneously avoiding the overlap of SBG reflection peak with the electronic absorption region.

4. Conclusion

In summary, this work presents the ability to control and tune the frequencies of slow photons generated from inverse opal TiO_2 photonic structures, in aqueous media, such that they can be efficiently harvested by the visible light-responsive $BiVO_4$ component of the heterocomposite for enhanced photocatalysis. Tuning of slow photons was realized by regulating the lattice parameter of the photonic structures (pore size) using different template sizes and by variation of light incidence angle from 0^o to 45^o in steps of 15^o using an optical fibre mounted on an angled fibre holder. We observed that the photocatalytic efficiencies of the IO photonic structures, under accurate tuning of slow photon frequencies to the electronic absorption of

$BiVO_4$, reached up to 7 times higher than those of the non-IO compact films. These experimental results were further substantiated by RCWA reflectance and absorptance simulations, which revealed not only a close match between experimental and theoretical positions of SBG's and slow photons but also a strong correlation between tuning of slow photon frequencies and increased absorptance that justified the enhanced photocatalytic activity. Through this work, we demonstrated the first proof of concept of tuning slow photon frequencies in aqueous medium and transferring them from IO photonic structures (TiO_2) to visible light-active photocatalyst ($BiVO_4$), for achieving exceptional photocatalytic activity. We believe that our work would instigate further research to improve light manipulation and harvesting in IO photonic structures for visible light photocatalysis, thereby opening innovative pathways for sustainable energy applications.

Acknowledgement

The author acknowledges the support of the Europe Occidentale Francophone (EOF) and Andhra (India) Jesuit provinces in realizing this work. S. R. M. was supported by the Belgian National Fund for Scientific Research (FRS-FNRS) (91400/1.B.309.18F) and the Maturation Fund of the Walloon Region, as a Postdoctoral Researcher. This research used resources of the Chemistry of Inorganic Materials (CMI) laboratory, Lasers, Optics & Spectroscopies (LOS) Technology Platform (https://platforms.unamur.be/los), the Physico-Chemical Characterization (PC^2) Technology Platform (https://platforms.unamur.be/pc2) and the Electron Microscopy Service (SME) of UNamur (http://www.unamur.be/en/sevmel). SME is a member of the Morphology - Imaging (MORPH-IM) Technology Platform of UNamur.

References

(1) Kubacka, A.; Fernandez-Garcia, M.; Colon, G. Advanced nanoarchitectures for solar photocatalytic applications. *Chem. Rev.* **2012,** *112* (3), 1555.

(2) Meng, X.; Liu, L.; Ouyang, S.; Xu, H.; Wang, D.; Zhao, N.; Ye, J. Nanometals for solar-to-chemical energy conversion: from semiconductor-based photocatalysis to plasmon-mediated photocatalysis and photo-thermocatalysis. *Adv. Mater.* **2016,** *28* (32), 6781.

(3) Xu, C.; Anusuyadevi, P. R.; Aymonier, C.; Luque, R.; Marre, S. Nanostructured materials for photocatalysis. *Chem. Soc. Rev.* **2019,** *48* (14), 3868.

(4) Armstrong, E.; O'Dwyer, C. Artificial opal photonic crystals and inverse opal structures – fundamentals and applications from optics to energy storage. *J. Mater. Chem. C* **2015,** *3* (24), 6109.

(5) Likodimos, V. Photonic crystal-assisted visible light activated TiO_2 photocatalysis. *Appl. Catal. B* **2018,** *230*, 269.

(6) Joannopoulos, J. D.; Johnson, S. G.; Winn, J. N.; Meade, R. D. *Photonic crystals*; Princeton Univ. Press, 2011.

(7) John, S. Strong localization of photons in certain disordered dielectric superlattices. *Phys. Rev. Lett.* **1987,** *58* (23), 2486.

(8) Soukoulis, C. M. *Photonic crystals and light localization in the 21st century*; Springer Science & Business Media, 2012.

(9) Yablonovitch, E. Inhibited spontaneous emission in solid-state physics and electronics. *Phys. Rev. Lett.* **1987,** *58* (20), 2059.

(10) Baba, T. Slow light in photonic crystals. *Nature photonics* **2008,** *2* (8), 465.

(11) Collins, G.; Armstrong, E.; McNulty, D.; O'Hanlon, S.; Geaney, H.; O'Dwyer, C. 2D and 3D photonic crystal materials for photocatalysis and electrochemical energy storage and conversion. *Sci. Technol. Adv. Mater.* **2016,** *17* (1), 563.

(12) Curti, M.; Schneider, J.; Bahnemann, D. W.; Mendive, C. B. Inverse opal photonic crystals as a strategy to improve photocatalysis: underexplored questions. *J. Phys. Chem. Lett.* **2015,** *6* (19), 3903.

(13) Pietron, J. J.; DeSario, P. A. Review of roles for photonic crystals in solar fuels photocatalysis. *J. Photonics Energy* **2016,** *7,* (1).

(14) Zheng, X.; Zhang, L. Photonic nanostructures for solar energy conversion. *Energy Environ. Sci.* **2016,** *9* (8), 2511.

(15) Liu, J.; Zhao, H.; Wu, M.; Van der Schueren, B.; Li, Y.; Deparis, O.; Ye, J.; Ozin, G. A.; Hasan, T.; Su, B. L. Slow photons for photocatalysis and photovoltaics. *Adv. Mater.* **2017,** *29* (17), 1605349.

(16) Chen, J. I. L.; von Freymann, G.; Choi, S. Y.; Kitaev, V.; Ozin, G. A. Amplified photochemistry with slow photons. *Adv. Mater.* **2006,** *18* (14), 1915.

(17) Wu, M.; Jin, J.; Liu, J.; Deng, Z.; Li, Y.; Deparis, O.; Su, B.-L. High photocatalytic activity enhancement of titania inverse opal films by slow photon effect induced strong light absorption. *J. Mater. Chem. A* **2013,** *1* (48), 15491.

(18) Wu, M.; Liu, J.; Jin, J.; Wang, C.; Huang, S.; Deng, Z.; Li, Y.; Su, B.-L. Probing significant light absorption enhancement of titania inverse opal films for highly exalted photocatalytic degradation of dye pollutants. *Appl. Catal. B* **2014,** *150-151*, 411.

(19) Xie, H.; Li, Y.; Jin, S.; Han, J.; Zhao, X. Facile fabrication of 3D-ordered macroporous nanocrystalline iron oxide films with highly efficient visible light induced photocatalytic activity. *J. Phys. Chem. C* **2010,** *114* (21), 9706.

(20) Zhang, L.; Baumanis, C.; Robben, L.; Kandiel, T.; Bahnemann, D. Bi_2WO_6 inverse opals: facile fabrication and efficient visible-light-driven photocatalytic and photoelectrochemical water-splitting activity. *Small* **2011,** *7* (19), 2714.

(21) Liu, J.; Jin, J.; Li, Y.; Huang, H.-W.; Wang, C.; Wu, M.; Chen, L.-H.; Su, B.-L. Tracing the slow photon effect in a ZnO inverse opal film for photocatalytic activity enhancement. *J. Mater. Chem. A* **2014,** *2* (14).

(22) Curti, M.; Mendive, C. B.; Grela, M. A.; Bahnemann, D. W. Stopband tuning of TiO_2 inverse opals for slow photon absorption. *Mater. Res. Bull.* **2017,** *91*, 155.

(23) Curti, M.; Zvitco, G.; Grela, M. A.; Mendive, C. B. Angle dependence in slow photon photocatalysis using TiO_2 inverse opals. *Chem. Phys.* **2018,** *502*, 33.

(24) Shen, K.; Zhang, L.; Chen, X.; Liu, L.; Zhang, D.; Han, Y.; Chen, J.; Long, J.; Luque, R.; Li, Y.et al. Ordered macro-microporous metal-organic framework single crystals. *Science* **2018,** *359* (6372), 206.

(25) Phillips, K. R.; Shirman, T.; Shirman, E.; Shneidman, A. V.; Kay, T. M.; Aizenberg, J. Nanocrystalline precursors for the co-assembly of crack-free metal oxide inverse opals. *Adv. Mater.* **2018,** *30* (19), 1706329.

(26) Kumbhar, V. S.; Lee, H.; Lee, J.; Lee, K. Interfacial growth of the optimal $BiVO_4$ nanoparticles onto self-assembled WO_3 nanoplates for efficient photoelectrochemical water splitting. *J. Colloid Interface Sci.* **2019,** *557*, 478.

(27) Kim, D. J.; Hahn, S. H.; Oh, S. H.; Kim, E. J. Influence of calcination temperature on structural and optical properties of TiO_2 thin films prepared by sol–gel dip coating. *Mater. Lett.* **2002,** *57* (2), 355.

(28) Hernández, S.; Thalluri, S. M.; Sacco, A.; Bensaid, S.; Saracco, G.; Russo, N. Photo-catalytic activity of $BiVO_4$ thin-film electrodes for solar-driven water splitting. *Appl. Cat. A-Gen.* **2015,** *504*, 266.

(29) Du, X.; He, J. Facile size-controllable syntheses of highly monodisperse polystyrene nano- and microspheres by polyvinylpyrrolidone-mediated emulsifier-free emulsion polymerization. *J. Appl. Polym. Sci.* **2008,** *108* (3), 1755.

(30) Gonzalez-Urbina, L.; Baert, K.; Kolaric, B.; Perez-Moreno, J.; Clays, K. Linear and nonlinear optical properties of colloidal photonic crystals. *Chem. Rev.* **2012,** *112* (4), 2268.

(31) Fattakhova-Rohlfing, D.; Zaleska, A.; Bein, T. Three-dimensional titanium dioxide nanomaterials. *Chem. Rev.* **2014,** *114* (19), 9487.

(32) Wei, Y.; Jiao, J.; Zhao, Z.; Liu, J.; Li, J.; Jiang, G.; Wang, Y.; Duan, A. Fabrication of inverse opal TiO_2-supported Au@ CdS core–shell nanoparticles for efficient photocatalytic CO_2 conversion. *Appl. Catal. B* **2015,** *179*, 422.

(33) Galisteo-López, J.; Palacios-Lidón, E.; Castillo-Martínez, E.; López, C. Optical study of the pseudogap in thickness and orientation controlled artificial opals. *Phys. Rev. B* **2003,** *68* (11), 115109.

(34) Jiang, P.; Bertone, J.; Hwang, K. S.; Colvin, V. Single-crystal colloidal multilayers of controlled thickness. *Chem. Mater.* **1999,** *11* (8), 2132.

(35) Schroden, R. C.; Al-Daous, M.; Blanford, C. F.; Stein, A. Optical properties of inverse opal photonic crystals. *Chem. Mater.* **2002,** *14* (8), 3305.

(36) Joannopoulos, J. D.; Johnson, S. G.; Winn, J. N.; Meade, R. D. *Molding the flow of light*; Princeton Univ. Press, 2008.

(37) Deparis, O.; Ghazzal, M.; Simonis, P.; Mouchet, S.; Kebaili, H.; De Coninck, J.; Gaigneaux, E. M.; Vigneron, J.-P. Theoretical condition for transparency in mesoporous layered optical media: application to switching of hygrochromic coatings. *Appl. Phys. Lett.* **2014,** *104* (2), 023704.

(38) Choy, T. C. *Effective medium theory: principles and applications*; Oxford Univ. Press, 2015.

(39) Park, Y. R.; Kim, K. J. Structural and optical properties of rutile and anatase TiO_2 thin films: effects of Co doping. *Thin Solid Films* **2005,** *484* (1-2), 34.

(40) Yuan, Y.; Huang, Y.; Ma, F.; Zhang, Z.; Wei, X. Effects of oxygen vacancy on the mechanical, electronic and optical properties of monoclinic $BiVO_4$. *J. Mater. Sci.* **2017,** *52* (14), 8546.

(41) Ottermann, C.; Bange, K. Correlation between the density of TiO_2 films and their properties. *Thin Solid Films* **1996,** *286* (1-2), 32.

(42) Sarkar, S.; Das, N.; Chattopadhyay, K. Optical constants, dispersion energy parameters and dielectric properties of ultra-smooth nanocrystalline $BiVO_4$ thin films prepared by rf-magnetron sputtering. *Solid State Sci.* **2014,** *33*, 58.

(43) Deparis, O.; Mouchet, S.; Su, B.-L. Light harvesting in photonic crystals revisited: why do slow photons at the blue edge enhance absorption? *Phys. Chem. Chem. Phys.* **2015,** *17* (45), 30525.

(44) Zhao, H.; Hu, Z.; Liu, J.; Li, Y.; Wu, M.; Van Tendeloo, G.; Su, B.-L. Blue-edge slow photons promoting visible-light hydrogen production on gradient ternary 3DOM TiO_2-Au-CdS photonic crystals. *Nano Energy* **2018,** *47*, 266.

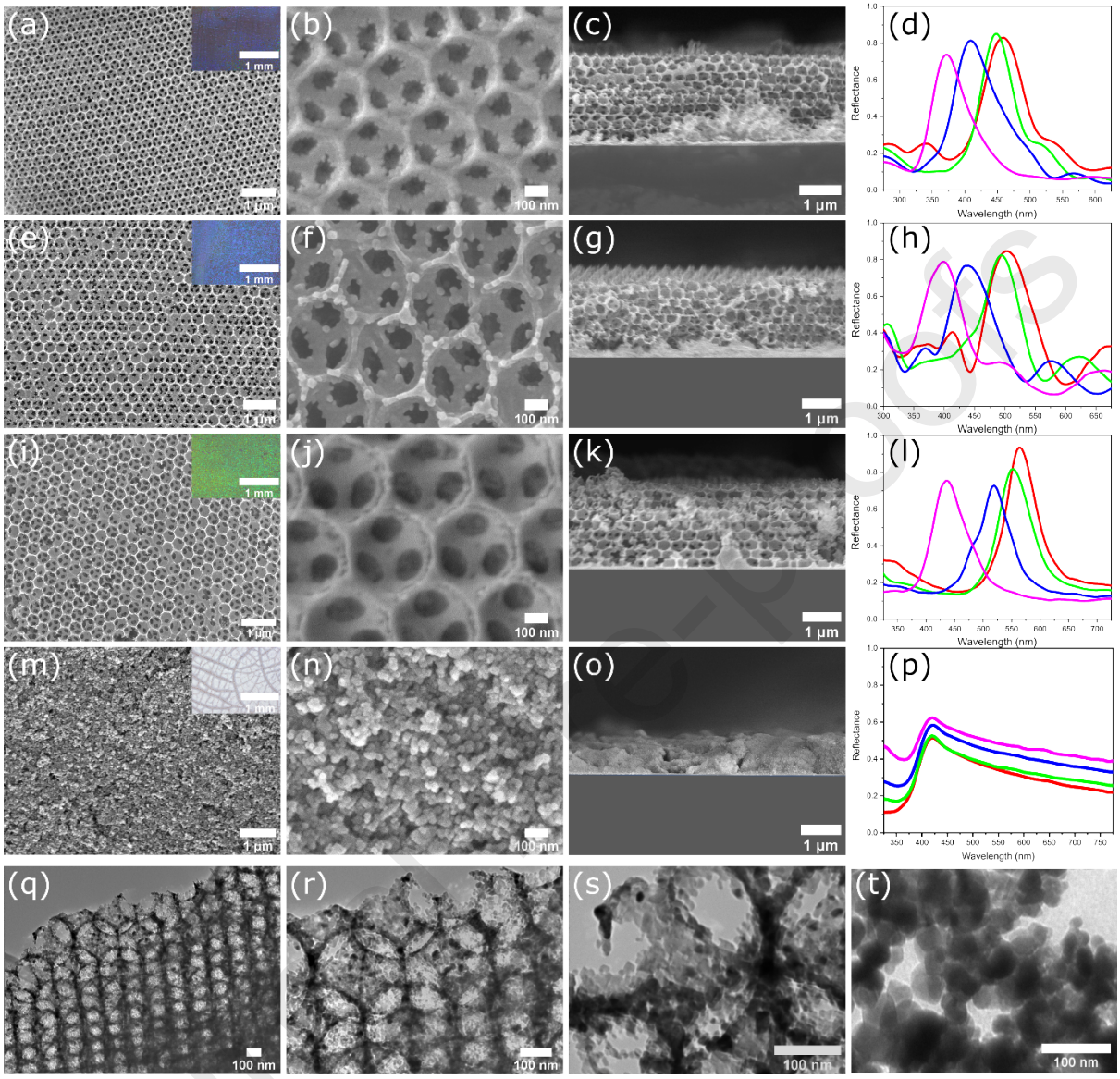

Fig. 1: Top view and cross section SEM images of inverse opal TiO_2 samples along with their corresponding optical microscope images (inset) and angle-resolved reflectance spectra in air at 0° (red), 15° (green), 30° (blue) and 45° (magenta) of: **(a-d)** IT 370, **(e-h)** IT 420, **(i-l)** IT 460 and **(m-p)** TiO_2 film respectively; **(q-s)** TEM images of IT 370 at different magnifications and **(t)** TEM image of TiO_2 film.

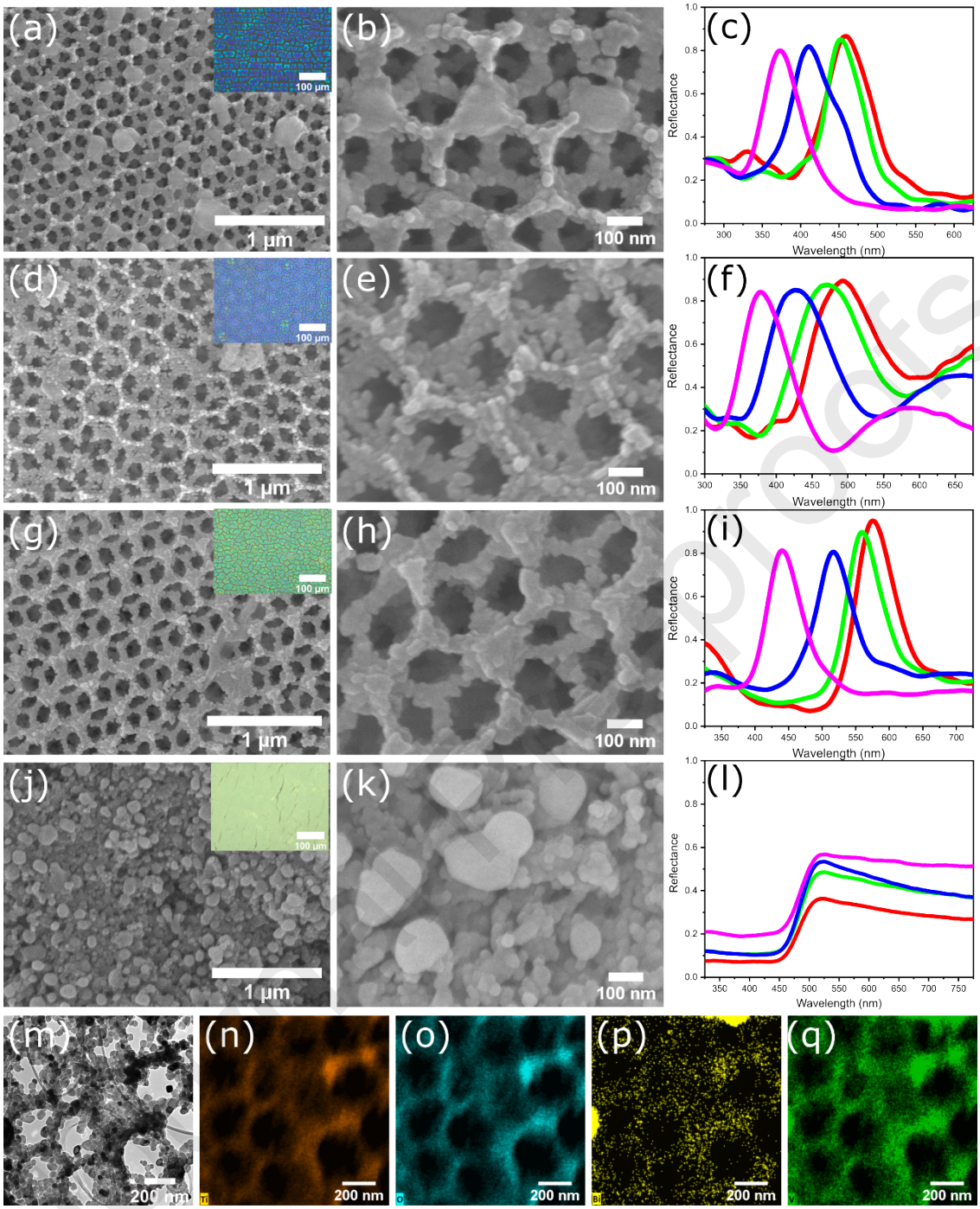

Fig. 2: SEM images of inverse opal TiO_2 samples after $BiVO_4$ deposition along with their corresponding optical microscope images (inset) and angle-resolved reflectance spectra in air at 0° (red), 15° (green), 30° (blue) and 45° (magenta) of: **(a-c)** ITBV 370, **(d-f)** ITBV 420, **(g-i)** ITBV 460, **(j-l)** TiO_2-$BiVO_4$ film, **(m-q)** TEM image of ITBV 370 (m), EDS mapping of Ti (n), O (o), Bi (p) and V (q).

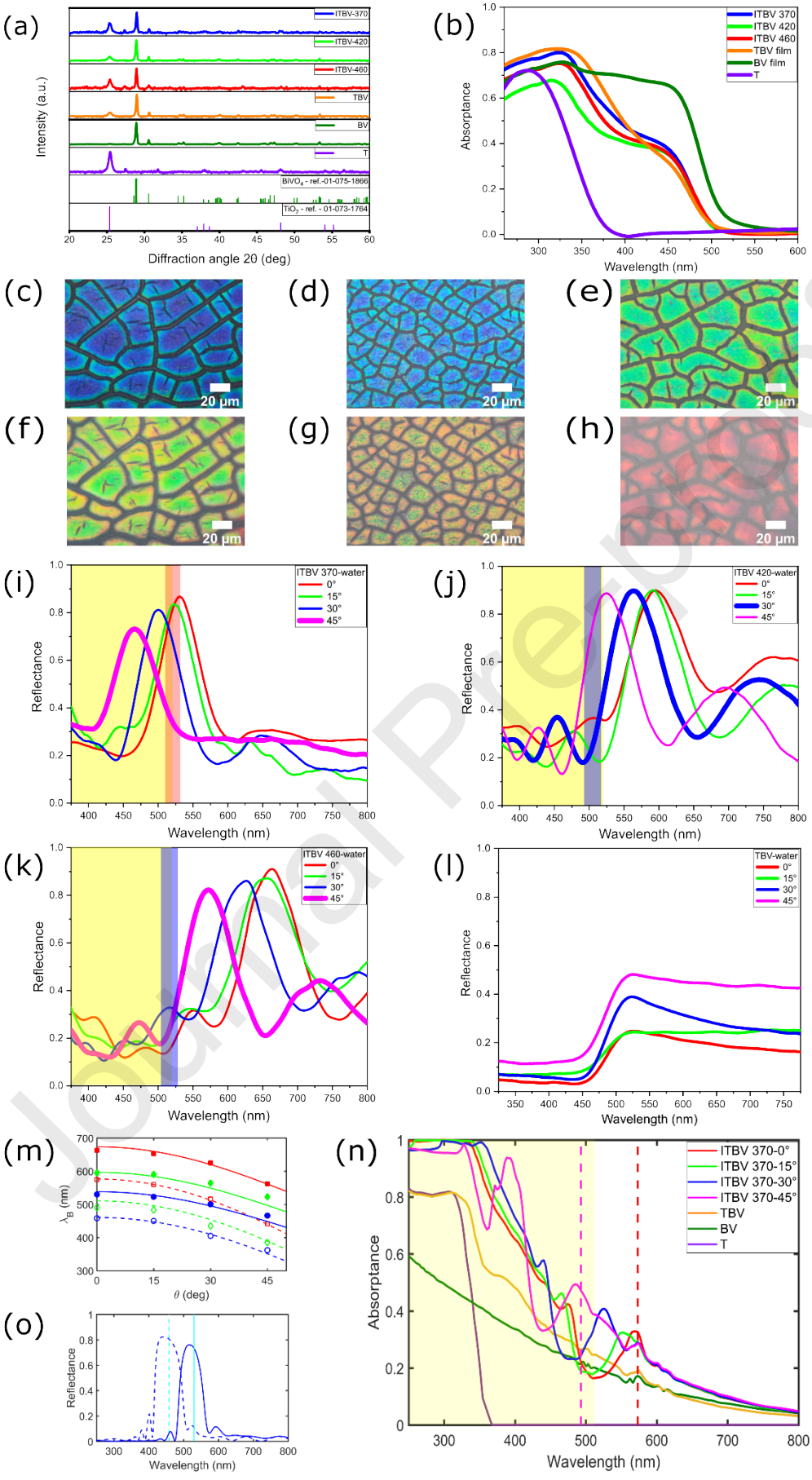

Fig. 3: (a) XRD patterns of (from top to bottom): IO TiO_2 deposited with $BiVO_4$: ITBV 370, ITBV 420, ITBV 460, TiO_2-$BiVO_4$ film (TBV), $BiVO_4$ film (BV), TiO_2 film (T); monoclinic $BiVO_4$ as reference and anatase TiO_2 as reference; **(b)** The corresponding UV-Visible absorbtance spectra of the same samples shown in (a); **(c-f)** Angle-resolved reflectance measurements in water of ITBV 370, ITBV 420, ITBV 460 and TiO_2-$BiVO_4$ film; yellow shade indicates the dominant electronic absorption region of $BiVO_4$; red shade in (c) refers to red edge slow photons of ITBV 370 at 45° while blue shades in (d, e) refer to blue edge slow photons of ITBV 420 at 30° and ITBV 460 at 45°; **(g-l)** Optical microscope images of the same area of ITBV samples in air and in water of ITBV 370 (g, j), ITBV 420 (h, k)and ITBV 460 (i, l); **(m)** Bragg law approximation of SBG reflectance peak position (λ_B) in air (dotted lines) and in water (solid lines) of ITBV 370 (blue), ITBV 420 (green) and ITBV 460 (red); experimental measurement of reflectance of the same samples are indicated by open dots (air) and closed dots (water); **(n)** RCWA simulation of absorptance of ITBV 370 in water at 0° (red), 15° (green), 30° (blue) and 45° (magenta), TiO_2-$BiVO_4$ thin film (orange), $BiVO_4$ thin film (green), and TiO_2 thin film (violet); corresponding dotted lines indicate red edge slow photon regions at 0° (red) and 45° (magenta) **(o)** RCWA simulation of the reflectance of ITBV 370 (o) at normal incidence in air (dash plot) and in water (line plot) with the corresponding lines indicating position of experimental SBG peaks.

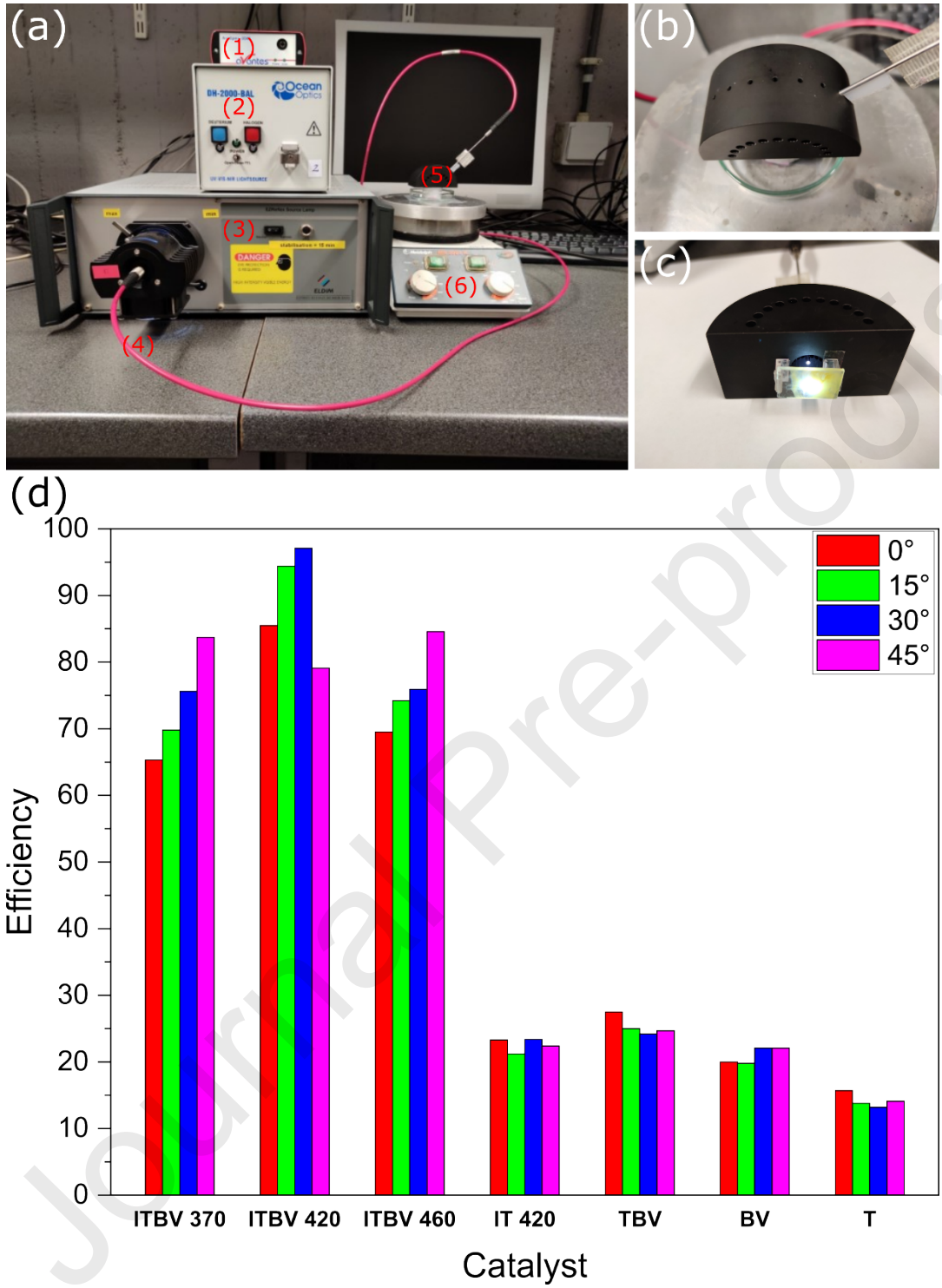

Fig. 4: Experimental set up for angle-resolved reflectance measurement and angle-resolved photocatalytic activity: (1) Spectrophotometer for reflectance measurement (2) Light source for angle-resolved reflectance measurement (3) Light source for photodegradation (4) Optical fibre for photodegradation (bifurcated optical fibre for reflectance measurement is not shown here) (5) Optical fibre holder (6) Magnetic stirrer **(b)** Top-view of optical fibre holder **(c)** Side-view of optical fibre holder with the photocatalyst fixed at the bottom **(d)** Comparison of the photocatalytic RhB degradation efficiency of: ITBV 370, ITBV 420, ITBV 460, IO TiO_2 (IT 420), TiO_2-$BiVO_4$ thin film (TBV), $BiVO_4$ thin film (BV) and TiO_2 thin film (T) at 0°, 15°, 30° and 45°.

Thomas Lourdu Madanu: Conceptualization, Methodology, Investigation, Formal analysis, Writing-original draft preparation. **Sebastien Mouchet:** Formal analysis, Writing-review & editing. **Olivier Deparis:** Formal analysis, Resources, **Jing Liu**: Writing-review & editing, **Yu Li**: Writing-review & editing, **Bao-Lian Su:** Conceptualization, Supervision, Visualization, Project administration.

Declaration of interests

☒ The authors declare that they have no known competing financial interests or personal relationships that could have appeared to influence the work reported in this paper.

☐The authors declare the following financial interests/personal relationships which may be considered as potential competing interests: